Article

Antarctic icebergs reorganize ocean circulation during Pleistocene glacials

https://doi.org/10.1038/s41586-020-03094-7

Received: 21 January 2020

Accepted: 20 October 2020

Published online: 13 January 2021

Check for updates

Aidan Starr[1]✉, Ian R. Hall[1]✉, Stephen Barker[1], Thomas Rackow[2], Xu Zhang[3,4], Sidney R. Hemming[5], H. J. L. van der Lubbe[1,6], Gregor Knorr[2], Melissa A. Berke[7], Grant R. Bigg[8], Alejandra Cartagena-Sierra[7], Francisco J. Jiménez-Espejo[9,10], Xun Gong[2,11], Jens Gruetzner[2], Nambiyathodi Lathika[12], Leah J. LeVay[13], Rebecca S. Robinson[14], Martin Ziegler[15] & Expedition 361 Science Party*

The dominant feature of large-scale mass transfer in the modern ocean is the Atlantic meridional overturning circulation (AMOC). The geometry and vigour of this circulation influences global climate on various timescales. Palaeoceanographic evidence suggests that during glacial periods of the past 1.5 million years the AMOC had markedly different features from today[1]; in the Atlantic basin, deep waters of Southern Ocean origin increased in volume while above them the core of the North Atlantic Deep Water (NADW) shoaled[2]. An absence of evidence on the origin of this phenomenon means that the sequence of events leading to global glacial conditions remains unclear. Here we present multi-proxy evidence showing that northward shifts in Antarctic iceberg melt in the Indian–Atlantic Southern Ocean (0–50° E) systematically preceded deep-water mass reorganizations by one to two thousand years during Pleistocene-era glaciations. With the aid of iceberg-trajectory model experiments, we demonstrate that such a shift in iceberg trajectories during glacial periods can result in a considerable redistribution of freshwater in the Southern Ocean. We suggest that this, in concert with increased sea-ice cover, enabled positive buoyancy anomalies to 'escape' into the upper limb of the AMOC, providing a teleconnection between surface Southern Ocean conditions and the formation of NADW. The magnitude and pacing of this mechanism evolved substantially across the mid-Pleistocene transition, and the coeval increase in magnitude of the 'southern escape' and deep circulation perturbations implicate this mechanism as a key feedback in the transition to the '100-kyr world', in which glacial–interglacial cycles occur at roughly 100,000-year periods.

In the modern ocean, the AMOC is characterized by the deep, southward spread of NADW towards the Southern Ocean, balanced by the northward return of surface, mode, intermediate and bottom waters[3,4]. Although the widely documented shoaling of NADW during Pleistocene glacial periods has previously been explained through changes in North Atlantic Ocean processes[5], this paradigm has been challenged by studies invoking 'upstream' disruptions (for example, variable Agulhas Leakage)[6,7]. Such disruptions would modify the shallow return of waters to the North Atlantic required to complete this 'upper cell' of the overturning circulation. Furthermore, the southward- and northward-spreading components of the upper cell are connected via wind- and buoyancy-related processes in the Southern Ocean, with much of the outcropping NADW first taking an indirect route, via the so-called 'lower cell' of overturning circulation, before joining the AMOC return limb via the upper cell[4] (Extended Data Fig. 1). Southern Ocean conditions have therefore been increasingly invoked by modelling studies[7–9] as key in setting NADW dynamics; however, palaeoceanographic evidence supporting such a causal link remains scarce[10].

Here we show a tight surface water–deep water coupling between the presence of far-travelled Antarctic icebergs and deep-water mass structure at the northern limit of the modern Subantarctic Zone (SAZ) during the past 1.65 million years (Myr). We examine new and previously published records of ice-rafted debris (IRD) mass-accumulation

[1]School of Earth and Environmental Sciences, Cardiff University, Cardiff, UK. [2]Alfred Wegener Institute, Helmholtz Centre for Polar and Marine Research, Bremerhaven, Germany. [3]Center for Pan Third Pole Environment (Pan-TPE), Key Laboratory of Western China's Environmental Systems, (Ministry of Education), College of Earth and Environmental Science, Lanzhou University, Lanzhou, China. [4]CAS Center for Excellence in Tibetan Plateau Earth Sciences, Chinese Academy of Sciences (CAS), Beijing, China. [5]Department of Earth and Environmental Sciences, Lamont-Doherty Earth Observatory of Columbia University, Palisades, NY, USA. [6]Faculty of Science, Vrije University, Amsterdam, The Netherlands. [7]Department of Civil and Environmental Engineering and Earth Sciences, University of Notre Dame, Notre Dame, IN, USA. [8]Department of Geography, University of Sheffield, Sheffield, UK. [9]Instituto Andaluz de Ciencias de la Tierra (CSIC-UGR), Armilla, Spain. [10]Research Institute for Marine Resources Utilization (Biogeochemistry Program), JAMSTEC, Yokosuka, Japan. [11]Hubei Key Laboratory of Marine Geological Resources, China University of Geosciences, Wuhan, China. [12]National Centre for Polar and Ocean Research, Ministry of Earth Sciences, Goa, India. [13]International Ocean Discovery Program, Texas A&M University, College Station, TX, USA. [14]Graduate School of Oceanography, University of Rhode Island, Narragansett, RI, USA. [15]Department of Earth Sciences, Utrecht University, Utrecht, The Netherlands. *A list of members and their affiliations appears at the end of the paper. ✉e-mail: StarrA1@Cardiff.ac.uk; Hall@Cardiff.ac.uk

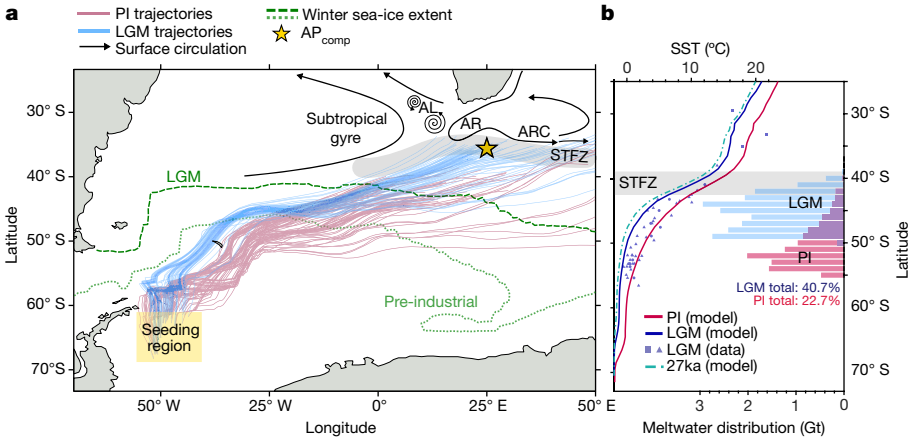

Fig. 1 | Modelled iceberg trajectories and meridionally averaged SST and meltwater distribution for the pre-industrial and LGM Atlantic Southern Ocean. a, Iceberg trajectories simulated by Pyberg for pre-industrial (PI) and last glacial maximum (LGM) conditions (see Methods). Winter sea-ice extent (percentage concentration contour for September from refs. [15,26]) is shown for pre-industrial and LGM. Surface ocean circulation is modified from ref. [3]. AR, Agulhas Retroflection; AL, Agulhas Leakage; ARC, Agulhas Return Current. The shaded grey band represents the subtropical frontal zone (STFZ)[51]. **b**, 0–50° E zonal mean of mean SST under pre-industrial (pink) and LGM (blue) conditions. SST proxy data are from MARGO[26] (blue symbols; triangles, diatom; circles, radiolarian; squares, alkenone). Model SST data are from COSMOS experiments (see Methods). The estimated meltwater distribution is given as total meltwater input in the 0–50° E zone as simulated by Pyberg (Methods); the values for pre-industrial (pink) and LGM (blue) are the percentage of the total initial iceberg mass (added as icebergs in the yellow 'seeding region' in **a**) that melts in the region. The map in **a** was produced using the M_Maps package for Matlab (http://www.eoas.ubc.ca/~rich/map.html).

rate[11,12] (IRD_{MAR}), and carbon and oxygen isotope records[13] from benthic foraminifera ($\delta^{13}C_{benthic}$, $\delta^{18}O_{benthic}$) from a new composite record of sediment cores recovered from the Agulhas Plateau in the south-west Indian Ocean. Spanning the past 1.65 Myr, the 'Agulhas Plateau composite' (hereafter AP_{comp}; see Methods for age model and composite construction) consists of MD02-2588 (41° 19.90′ S, 25° 49.70′ E, 2,907 m water depth) and International Ocean Discovery Program (IODP) site U1475 (41° 25.60′ S, 25° 15.60′ E, 2,669 m water depth).

Iceberg tracks and deep hydrography

The Agulhas Plateau is situated at the southern boundary of the Indian–Atlantic Ocean Gateway (Fig. 1a); the upper water column is dominated by eastward-flowing Indian Ocean surface waters retroflected as the Agulhas Return Current (that is, not 'leaked' into the South Atlantic). To the south, the relatively cold and fresh waters of the SAZ meet their northern limit, forming steep hydrographic gradients at the subtropical frontal zone (STFZ; Fig. 1). Iceberg presence (and subsequently IRD deposition) at this location can therefore be influenced by regional hydrography (that is, shifts in the STFZ) as well as the export, survivability and transport of icebergs into and across the Southern Ocean. To aid in our interpretation of the IRD_{MAR} proxy, we perform iceberg-trajectory modelling experiments using Pyberg, an offline implementation of the Finite Element Sea Ice-Ocean Model (FESOM-IB)[14] iceberg drift and decay module. We force Pyberg with the Community Earth System Models (COSMOS)[15] run to quasi-equilibrium under pre-industrial and last glacial maximum (LGM) climate conditions (see Methods). In each experiment, 111 icebergs were seeded from observationally derived locations in the Weddell Sea 'iceberg alley' (Methods; shaded box in Fig. 1a) and are treated as passive particles, moving and decaying according to oceanic (including sea-ice) and atmospheric conditions. In reality, the mass balance and discharge of icebergs from the Antarctic Ice Sheet was probably variable in the past; however, by initializing these experiments with consistent iceberg seeding, and neglecting a possible subantarctic source of icebergs[16] (on the petrological grounds outlined in Methods), we are able to assess the relative redistribution of iceberg melt resulting only from changes in Southern Ocean conditions.

Much as the surface hydrography at the Agulhas Plateau represents a junction between subantarctic and subtropical regimes, the deep circulation is characterized by competing northern- and southern-sourced water masses (NSW and SSW, respectively). NSW here refers to NADW, and glacial analogues, which today extends to 3,000 m water depth as it exits the Atlantic Ocean into the Southern Ocean[3]. A weakening and shoaling of NSW, as in some glacial reconstructions[2], would result in increased presence of SSW at the Agulhas Plateau, consisting of some combination of Lower Circumpolar Deep Water and Antarctic Bottom Water, flowing clockwise around the Southern Ocean, and spreading northwards into the neighbouring subtropical basins[4]. We examine the relative contribution of NSW versus SSW at the Agulhas Plateau through the $\delta^{13}C$ of *Cibicidoides wuellerstorfi*, an epifaunal benthic foraminifer, shown previously to be closely related to the $\delta^{13}C_{DIC}$ of ambient seawater[17], and therefore a widely applied proxy to trace past changes in deep ocean ventilation by ocean circulation[1,2].

As with the IRD proxy, the $\delta^{13}C_{benthic}$ record may be influenced by numerous environmental processes. In other words, it is not a simple water-mass tracer, and may be affected additionally by productivity signals[18] and non-stationary water-mass end-members[19]. After accounting for time-varying end-member signatures using a binary mixing model (Extended Data Fig. 4) we find that the %NSW is well correlated with the raw $\delta^{13}C_{benthic}$ record at the AP_{comp} ($r^2 = 0.39$), supporting our interpretation that relative NSW versus SSW presence at the site is the dominant control on $\delta^{13}C_{benthic}$. This inference is in agreement with complementary water-mass tracers[20] and basin-wide data compilations and modelling studies[2]. The timing of $\delta^{13}C_{benthic}$ changes recorded in the AP_{comp} can therefore be instructive in identifying the origin of deep circulation changes with respect to surface Southern Ocean conditions recorded in the co-registered IRD_{MAR} data.

Surface–deep phasing

The glacial AP_{comp} is characterized by generally higher IRD_{MAR} and lower $\delta^{13}C_{benthic}$ (shaded bars in Fig. 2) compared to interglacials, reflecting the increased presence of Antarctic icebergs and the reduced presence of NSW, respectively. A significant negative correlation is present between IRD_{MAR} and $\delta^{13}C_{benthic}$ ($r^2 = -0.39$), becoming stronger still when IRD_{MAR} is log-transformed ($r^2 = -0.54$). The reason for log-transforming the IRD_{MAR} data is twofold: first, it has a strongly skewed distribution with a small number of very high values. Second, we consider log-IRD_{MAR}

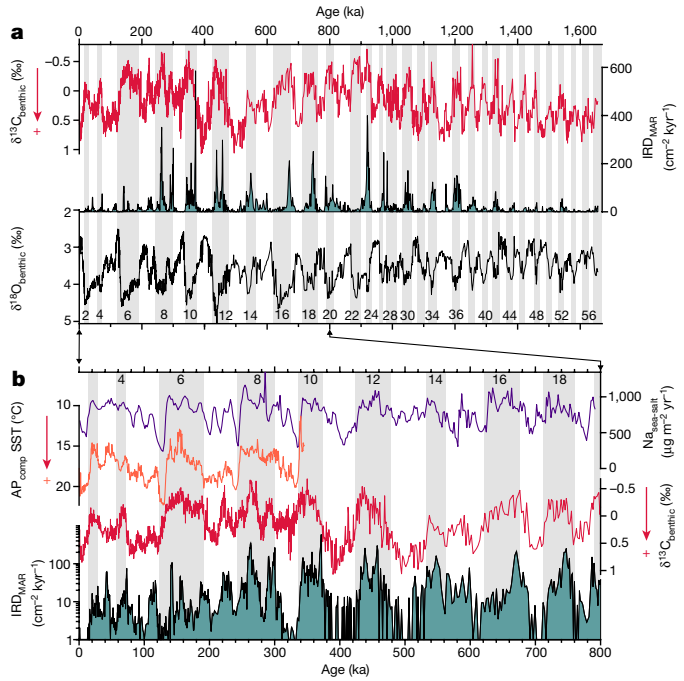

Fig. 2 | Palaeoceanographic proxy records from the mid-to-late Pleistocene AP_{comp}. **a**, Time series of $\delta^{13}C_{benthic}$ (top; pink; note reversed scale), IRD_{MAR} (middle; teal), and $\delta^{18}O_{benthic}$ (lower; grey; note reversed scale) from the AP_{comp} for the past 1.65 Myr, with glacial MISs shaded grey and labelled at bottom. The interval 0–800 ka is magnified in **b**, and additionally includes the $Na_{sea\text{-}salt}$ accumulation from the EPICA Dome C Antarctic ice core[27], a proxy for Southern Ocean sea-ice extent (top, purple). The AP_{comp} alkenone unsaturation index ($U^{k'}_{37}$) SST record from ref. [46] is also shown (second from top, orange). Note the log scale for IRD_{MAR} in **b**.

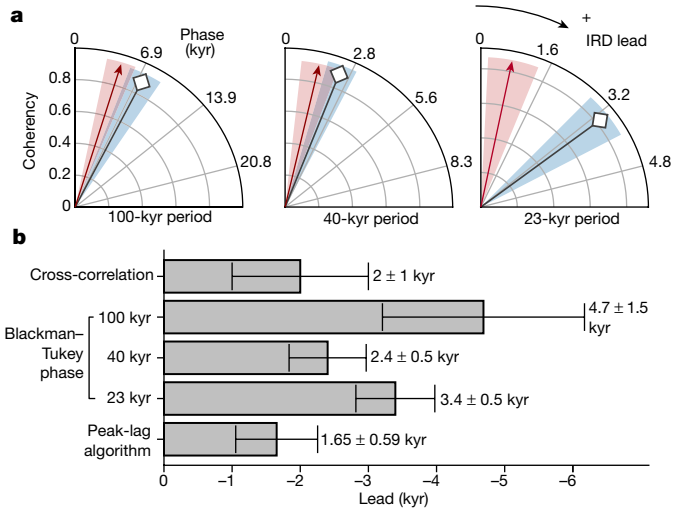

Fig. 3 | IRD_{MAR} versus $\delta^{13}C_{benthic}$ lead–lag relationship. **a**, Blackman–Tukey coherency phase of IRD_{MAR} against $\delta^{13}C_{benthic}$ (red; triangular-head arrows) and $\delta^{18}O_{benthic}$ (blue; diamond-head arrows) in the 100 kyr^{-1}, 40 kyr^{-1} and 23 kyr^{-1} frequency bands. These phase wheels are cropped at 0–90°, with clockwise rotation indicating a larger lead for IRD_{MAR} (given in kyr on the curved axes). The arrow length represents coherency and the shaded areas give the 95% uncertainty in phase. IRD_{MAR} leads $\delta^{13}C_{benthic}$ and $\delta^{18}O_{benthic}$ in phase for all three frequencies. **b**, Summary of lead times for IRD_{MAR} over $\delta^{13}C_{benthic}$ determined by three independent approaches, with estimates of 95% uncertainty given by the black bars (see Methods).

a more sensitive indicator of palaeo-iceberg drift—for example the probability of iceberg presence in the Southern Ocean decreases exponentially with distance north of the main iceberg belt in the Weddell Sea sector[21]. To explore the phasing of the close relationship between the co-registered surface and deep AP_{comp} conditions we use three independent approaches. The strongest correlation between the two records ($r^2 = -0.59$) occurs when IRD_{MAR} leads $\delta^{13}C_{benthic}$ by 2 ± 1 kyr (Extended Data Fig. 5d), and spectral coherency analysis reveals a lead for IRD_{MAR} in all three major Milankovitch frequency bands (Fig. 3a). Additionally, a numerical algorithm which determines the offsets between peaks in rate of change reveals that maxima in the IRD_{MAR} occur on average 1.65 ± 0.59 kyr before maxima in the rate of $\delta^{13}C_{benthic}$ decrease (Fig. 3b). Together, these approaches independently demonstrate that IRD_{MAR} systematically leads $\delta^{13}C_{benthic}$ at the AP_{comp}; the unidirectional result from the 'peak-lag algorithm' best allows us to quantify this lead as 1–2 kyr, providing a valuable constraint on the link between the Southern Ocean surface variability and deep-water mass geometry during transitions from interglacial to glacial conditions over the past 1.65 Myr.

Understanding this relationship further requires a robust interpretation of both the IRD_{MAR} and $\delta^{13}C_{benthic}$ proxies. For example, we might interpret higher glacial IRD_{MAR} as indicating a glacial shift in iceberg trajectories. This interpretation is coherent with published IRD records, which show that deposition close to Antarctica is generally highest during interglacial periods[22,23] and periods of ice-sheet retreat[23,24] (for example, glacial terminations), whereas at SAZ locations IRD maxima typically occur during glacial periods (this study, and refs. [22,25]). From this we can deduce that glacial conditions in the Southern Ocean favour the increased transport of icebergs away from Antarctica (Fig. 1), as the early decay of icebergs is reduced and the overall survivability and transport enhanced, owing to cooler surface temperatures[26], increased sea ice[26,27], and changes in surface circulation, possibly relating to the westerly-wind belt. Iceberg drift in the ocean is associated with, and can facilitate, sea-ice formation[21], and sea-ice presence in turn can inhibit the wave-driven erosion of icebergs[28] and govern iceberg movement under severe ice conditions[29]. Enhanced sea-ice concentration and extent is a well documented feature of the glacial Southern Ocean[26], and the close correspondence between the AP_{comp} IRD_{MAR} record and an Antarctic ice-core proxy for sea-ice extent[27] (Fig. 2) over the past eight glacial cycles suggests that such a feedback may be important.

Furthermore, our modelling results indicate that LGM conditions are associated with an equatorward shift and lengthening of trajectories relative to pre-industrial (Fig. 1) and modern observations[30]. Although long-term IRD_{MAR} variability in the SAZ is probably influenced by varied calving rates, a dramatically altered distribution of icebergs does not require a substantial change to ice-sheet mass balance. We acknowledge, however, that iceberg presence and therefore IRD deposition at the AP_{comp} does require some calving of icebergs to occur, and therefore necessitates a sufficiently large ice sheet. Considering evidence that East Antarctica maintained a marine-terminating ice sheet across the warm interglacial marine isotope stage (MIS) 31[31], we reason that the calving-ice-sheet condition would have been consistently met during the glacial intervals relevant to our proposed mechanism[32].

The southern escape

In the modern ocean the conveyor of icebergs traversing the Southern Ocean constitutes a major transport of meteoric freshwater away from the Antarctic Ice Sheet, particularly in the Weddell Sea sector[33]: a sizeable fraction of modern iceberg mass (up to 35% for giant icebergs)[14,33] can be exported north of 63° S. By estimating iceberg meltwater inputs from our trajectory experiments (Methods), we find a substantial redistribution of freshwater in the Southern Ocean, as the latitude at which this meltwater is greatest shifts several degrees to the north under glacial conditions, with meltwater input south of 50° S diminishing (Fig. 1).

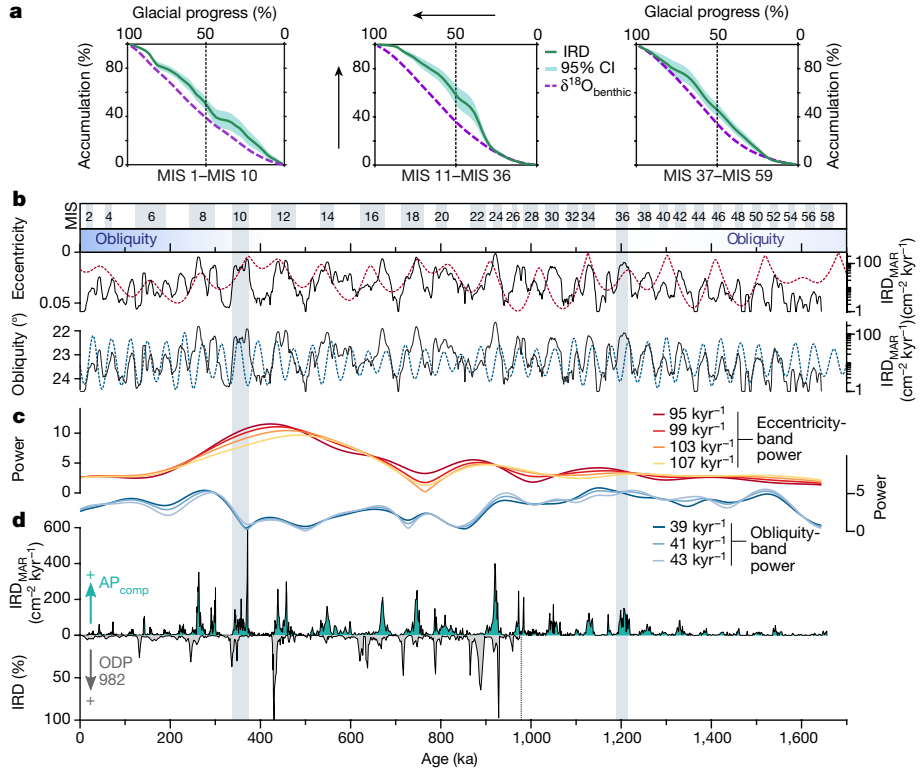

Fig. 4 | The evolution of the AP_{comp} IRD_{MAR} record in the time and frequency domain with respect to orbital forcing, global climate and inter-hemispheric phasing. a, Results from the 'glacial accumulation' analysis: IRD_{MAR} and $\delta^{18}O_{benthic}$ time series are divided into glacial intervals, then the cumulative integral is taken within each interval and normalized to 100% in time and value. 'Glacial progress %' refers to the relative time between the onset and termination of each glacial interval. 'Accumulation' refers to the normalized cumulative integral. For example, 50% indicates that half of the total IRD_{MAR} deposited in that cycle has been deposited; if this falls to the right of the $\delta^{18}O_{benthic}$ curve, it suggests that IRD_{MAR} is accumulating relatively early within the glacial (see Methods). The three panels show the average and 95% bootstrap confidence intervals (CI; standard error of the mean) for three periods: MIS 1 to MIS 10 (left), MIS 11 to MIS 36 (middle), and MIS 37 to MIS 59 (right). **b**, IRD_{MAR} on a log scale (black) with orbital eccentricity (red, dashed line) and orbital obliquity (blue, dashed line) from ref. [52]. Shaded grey bars (top) highlight glacial MISs, and the blue gradient bar (second from top) indicates periods with dominant obliquity pacing. **c**, Wavelet analysis (using a Mortlet wave with zero padding) of IRD_{MAR}, revealing the temporal evolution of relative power in the eccentricity (red-orange lines) and obliquity (blue lines) frequency bands. **d**, Inter-hemispheric comparison between the AP_{comp} IRD_{MAR} record (green; top) and a 1-Myr record of IRD (percentage IRD relative to planktonic foraminifera) from the North Atlantic site ODP 982[44] (bottom; grey; note reversed *y* axis).

Furthermore, we find nearly twice as much meltwater in the region between 0–50° E under LGM conditions compared to pre-industrial conditions (22.7% and 40.7% of the total initial iceberg mass, respectively; see Methods). Although this is clearly an idealized representation, with no change in calving rate imposed between experiments, it demonstrates that changes in Southern Ocean conditions can dramatically alter the buoyancy budget of the Southern Ocean. For example in the modern Southern Ocean, the meltwater associated with iceberg maxima can exceed the local precipitation-evaporation balance[14].

A connection between Southern Ocean surface forcing and the deep ocean has been explored through various theoretical lenses. A common theme occurs whereby enhanced sea-ice (formation and extent) results in an expansion of the region of net surface-buoyancy loss[8,9], owing to increased brine rejection close to, and subsequent melt occurring away from, the continent. However, the ability of sea-ice-buoyancy forcing alone to explain the full NSW shoaling implied by palaeoceanographic evidence has been questioned[34] and such a direct link is challenged by the failure of climate models without additional cooling in the Southern Ocean[15] to simulate a shoaled glacial NSW. We suggest that the equatorward shift in Antarctic iceberg melt, a feature absent from the aforementioned models, may be a key, previously unconsidered, component in connecting the surface Southern Ocean to overturning circulation. This would allow positive buoyancy anomalies to, in essence, 'escape' the Southern Ocean into the return AMOC limb; ultimately influencing deepwater formation in the upper (NSW) instead of the lower (SSW) overturning cell. The return limb of AMOC consists of surface to intermediate waters entering the South Atlantic gyre[4] through northward Ekman transport across the Southern Ocean and entrainment in the South Atlantic Subtropical Gyre, or via the shedding of warm and saline mesoscale eddies by the so-called Agulhas Leakage[35] (Fig. 1a). The importance of this return limb is illustrated by the role of Agulhas Leakage in the resumption of NADW formation at glacial terminations, when an increase in the inter-ocean exchange of salt transfers positive density anomalies into the Atlantic basin, triggering the resumption of a strong, deep AMOC mode[7,36]. The corollary would suggest that reducing the density export into the South Atlantic, for example through the 'southern escape' of iceberg meltwater, would have the inverse effect: suppressing NADW formation.

Such a mechanism finds support from Southern Ocean 'hosing' experiments which find that freshwater addition in the Southern Ocean (in these experiments, south of 60° S) can affect NADW formation[37,38], owing to Ekman spread of surface waters away from the Southern Ocean. However, these experiments also generate a weaker Lower Cell: the palaeoceanographic evidence for which remains equivocal. Although sea-ice formation may have stimulated the lower cell[39], grounded ice cover in coastal regions of AABW formation may have

had an opposing effect[32,40]. At the Agulhas Plateau, negative $\delta^{13}C_{benthic}$ excursions during glacial periods of the past 200 kyr are associated with increased near-bottom flow speeds[41], indicating a vigorous yet poorly ventilated glacial SSW (that is, lower overturning cell) consistent with increased SSW convection[10] fed by surface waters isolated from the atmosphere by enhanced sea ice[39]. That being said, the 1–2 kyr lag time observed here is difficult to reconcile with a direct Southern Ocean mechanism and the temporal offset between IRD_{MAR} and $\delta^{13}C_{benthic}$ may instead favour a teleconnection operating with a threshold behaviour. For example, although the northward export of icebergs to the SAZ would directly decrease the buoyancy flux in AABW formation regions, NADW formation may initially remain strong enough to prevent the northward/upward expansion of SSW. This would continue until the associated 'escape' of buoyancy anomalies into the upper cell has gradually weakened NADW formation across some threshold whereby the expansion of SSW into the deep Atlantic is possible.

Orbital pacing and sequence of events

With this mechanism in mind, we next examine the timing of events at the AP_{comp} in the context of global climate. In agreement with evidence for an early climate signal in the Southern Ocean during interglacial–glacial transitions[10,42,43] we find that IRD_{MAR} leads $\delta^{18}O_{benthic}$ at all three major orbital frequency bands (Fig. 3a). Under the assumption that $\delta^{18}O_{benthic}$ changes synchronously with global climate, this would imply that IRD_{MAR} peaks lead relative to global climate (or at least Northern Hemisphere ice volume). Moreover, a distinct inter-hemispheric asynchrony is suggested by the phasing of IRD between the Southern Ocean and the North Atlantic: IRD peaks at the AP_{comp} typically precede IRD peaks at ODP site 982[44] (Fig. 4d). A sequence of events emerges in which at the onset of glacial periods a northward expansion of Antarctic iceberg melt occurs, facilitated by increased sea-ice extent and surface cooling in the Southern Ocean[10], preceding the descent into full global glacial conditions as indicated by maxima in the global $\delta^{18}O_{benthic}$ record. The external forcing of this sequence of events may therefore be identified by the external forcing of SST and sea-ice in the Southern Ocean; a role for which obliquity has been invoked[45]. Indeed, we observe cooler surface conditions in our low obliquity model experiment (LGM27ka), compared to LGM (Extended Data Fig. 6), and find that icebergs travel further and decay more slowly between 'iceberg alley' and the Atlantic–Indian SAZ when obliquity is low. This is consistent with existing SST reconstructions from the Agulhas Plateau[46] showing colder SST during lower obliquity (Fig. 2b).

The pacing of IRD_{MAR} peaks by obliquity is apparent during cycles before approximately 1.2 Myr ago (Ma) (MIS 36) and after around 0.4 Ma (MIS 11; Fig. 4b); however, the pacing of the cycles is somewhat obscured during the mid-Pleistocene transition (MPT). During the MPT, the dominant cyclicity in IRD_{MAR} shifts from about 40 kyr^{-1} to 100 kyr^{-1}, possibly reflecting a transition to a nonlinear response to orbital forcing that is associated with larger ice sheets[47]. We note that the surface–deep lead (IRD_{MAR} versus $\delta^{13}C_{benthic}$) is mostly constant at 1–2 kyr for the entire 1.65-Myr record, however the lead of Southern Ocean processes over maxima in $\delta^{18}O_{benthic}$ (and hence glacial conditions) is variable, increasing between approximately 1.2 Ma and 0.4 Ma. For example, during MISs 24–26, greater than 80% of the total IRD_{MAR} accumulated within the first 50% of the glacial cycle (Fig. 4a). This is compared to approximately 60% accumulation by halfway through the pre- and post-MPT cycles. An increase in this lead of Southern Ocean processes over global ice volume may have resulted from growing larger ice sheets across the MPT (which would take longer to develop). The return to a shorter lead time in the late Pleistocene then implying that the rate of ice-sheet growth had increased to accommodate this larger size. Furthermore, glacial IRD_{MAR} maxima at the AP_{comp} increase across the MPT (Fig. 4d), beginning at MIS 36 (approximately 1.2 Ma) and probably reflecting enhanced export of icebergs across the SAZ, coincident with surface cooling and freshening in the Atlantic sector of the Southern Ocean[48].

Although this long-term trend may be driven by increasingly iceberg-favourable (cooler) conditions in the region[48], we cannot rule out a role for some change in the discharge of Antarctic icebergs amid a background of global cooling and possible transitions in the character of Antarctic ice sheets[49]. Regardless, the southern escape of freshwater (IRD_{MAR}) into the SAZ appears to scale with the magnitude of glacial AMOC perturbations as indicated by $\delta^{13}C_{benthic}$ minima; notably, the IRD_{MAR} maximum (and $\delta^{13}C_{benthic}$ minimum) at around 0.9 Ma coincides with the implied collapse in AMOC as recorded in the nearby deep Cape Basin[50]. This apparent scaling, as well as the consistent temporal coupling between the southern escape of freshwater and deep-water mass perturbations across this interval, implicate this feedback as a central ingredient in setting overturning circulation state across the MPT and in doing so, perhaps promoting the sequestration of atmospheric CO_2 during the longer glacial intervals of the 100-kyr world[19].

Online content

Any methods, additional references, Nature Research reporting summaries, source data, extended data, supplementary information, acknowledgements, peer review information; details of author contributions and competing interests; and statements of data and code availability are available at https://doi.org/10.1038/s41586-020-03094-7.

1. Lisiecki, L. E. Atlantic overturning responses to obliquity and precession over the last 3 Myr. *Paleoceanography* **29**, 71–86 (2014).
2. Hesse, T., Butzin, M., Bickert, T. & Lohmann, G. A model-data comparison of $\delta^{13}C$ in the glacial Atlantic Ocean. *Paleoceanography* **26**, PA3220 (2011).
3. Bower, A. et al. Lagrangian views of the pathways of the Atlantic meridional overturning circulation. *JGR Oceans* **124**, 5313–5335 (2019).
4. Talley, L. D. Closure of the global overturning circulation through the Indian, Pacific, and southern oceans. *Oceanography* **26**, 80–97 (2013).
5. Swingedouw, D., Braconnot, P., Delecluse, P., Guilyardi, E. & Marti, O. The impact of global freshwater forcing on the thermohaline circulation: adjustment of North Atlantic convection sites in a CGCM. *Clim. Dyn.* **28**, 291–305 (2007).
6. Caley, T., Giraudeau, J., Malaizé, B., Rossignol, L. & Pierre, C. Agulhas leakage as a key process in the modes of Quaternary climate changes. *Proc. Natl Acad. Sci. USA* **109**, 6835–6839 (2012).
7. Knorr, G. & Lohmann, G. Southern Ocean origin for the resumption of Atlantic thermohaline circulation during deglaciation. *Nature* **424**, 532–536 (2003).
8. Watson, A. J., Vallis, G. K. & Nikurashin, M. Southern Ocean buoyancy forcing of ocean ventilation and glacial atmospheric CO_2. *Nat. Geosci.* **8**, 861–864 (2015).
9. Ferrari, R. et al. Antarctic sea ice control on ocean circulation in present and glacial climates. *Proc. Natl Acad. Sci. USA* **111**, 8753–8758 (2014).
10. Govin, A. et al. Evidence for northward expansion of Antarctic Bottom Water mass in the Southern Ocean during the last glacial inception. *Paleoceanography* **24**, PA1202 (2009).
11. Marino, G. et al. Agulhas salt-leakage oscillations during abrupt climate changes of the Late Pleistocene. *Paleoceanography* **28**, 599–606 (2013).
12. Simon, M. H. et al. Millennial-scale Agulhas Current variability and its implications for salt-leakage through the Indian–Atlantic Ocean Gateway. *Earth Planet. Sci. Lett.* **383**, 101–112 (2013).
13. Ziegler, M., Diz, P., Hall, I. R. & Zahn, R. Millennial-scale changes in atmospheric CO_2 levels linked to the Southern Ocean carbon isotope gradient and dust flux. *Nat. Geosci.* **6**, 457–461 (2013).
14. Rackow, T. et al. A simulation of small to giant Antarctic iceberg evolution: differential impact on climatology estimates. *JGR Oceans* **122**, 3170–3190 (2017).
15. Zhang, X., Lohmann, G., Knorr, G. & Xu, X. Different ocean states and transient characteristics in last glacial maximum simulations and implications for deglaciation. *Clim. Past* **9**, 2319–2333 (2013).
16. Bigg, G. R. The impact of icebergs of sub-Antarctic origin on Southern Ocean ice-rafted debris distributions. *Quat. Sci. Rev.* **232**, 106204 (2020).
17. Schmittner, A. et al. Calibration of the carbon isotope composition ($\delta^{13}C$) of benthic foraminifera. *Paleoceanography* **32**, 512–530 (2017).
18. Mackensen, A. & Licari, L. Carbon isotopes of live benthic foraminifera from the South Atlantic: sensitivity to bottom water carbonate saturation state and organic matter rain rates. In *The South Atlantic in the Late Quaternary* (eds Wefer, G. et al.) 623–644 (Springer, 2003).
19. Lear, C. H. et al. Breathing more deeply: deep ocean carbon storage during the mid-Pleistocene climate transition. *Geology* **44**, 1035–1038 (2016).
20. Howe, J. N. & Piotrowski, A. M. Atlantic deep water provenance decoupled from atmospheric CO_2 concentration during the lukewarm interglacials. *Nat. Commun.* **8**, 2003 (2017).
21. Merino, N. et al. Antarctic icebergs melt over the Southern Ocean: climatology and impact on sea ice. *Ocean Model.* **104**, 99–110 (2016).
22. Keany, J., Ledbetter, M., Watkins, N. & Huang, T. C. Diachronous deposition of ice-rafted debris in sub-Antarctic deep-sea sediments. *Bull. Geol. Soc. Am.* **87**, 873–882 (1976).

23. Diekmann, B. et al. Terrigenous sediment supply in the polar to temperate South Atlantic: land–ocean links of environmental changes during the Late Quaternary. In *The South Atlantic in the Late Quaterna*ry (eds Wefer, G. et al.) 375–399 (Springer, 2003).
24. Weber, M. E. et al. Millennial-scale variability in Antarctic ice-sheet discharge during the last deglaciation. *Nature* **510**, 134–138 (2014).
25. Teitler, L. et al. Determination of Antarctic Ice Sheet stability over the last ~500 ka through a study of iceberg-rafted debris. *Paleoceanography* **25**, PA1202 (2010).
26. Gersonde, R., Crosta, X., Abelmann, A. & Armand, L. Sea-surface temperature and sea ice distribution of the Southern Ocean at the EPILOG Last Glacial Maximum – a circum-Antarctic view based on siliceous microfossil records. *Quat. Sci. Rev*. **24**, 869–896 (2005).
27. Wolff, E. W. et al. Southern Ocean sea-ice extent, productivity and iron flux over the past eight glacial cycles. *Nature* **440**, 491–496 (2006).
28. Wagner, T. J. et al. Wave inhibition by sea ice enables trans-Atlantic ice rafting of debris during Heinrich events. *Earth Planet. Sci. Lett*. **495**, 157–163 (2018).
29. Schodlok, M. P., Hellmer, H. H., Rohardt, G. & Fahrbach, E. Weddell Sea iceberg drift: five years of observations. *JGR Oceans* **111**, C06018 (2006).
30. Tournadre, J., Bouhier, N., Girard-Ardhuin, F. & Rémy, F. Antarctic icebergs distributions 1992–2014. *JGR Oceans* **121**, 327–349 (2016).
31. Teitler, L. et al. Antarctic Ice Sheet response to a long warm interval across Marine Isotope Stage 31: a cross-latitudinal study of iceberg-rafted debris. *Earth Planet. Sci. Lett*. **409**, 109–119 (2015).
32. Pollard, D. & DeConto, R. M. Modelling West Antarctic ice sheet growth and collapse through the past five million years. *Nature* **458**, 329–332 (2009).
33. Silva, T. A., Bigg, G. R. & Nicholls, K. W. Contribution of giant icebergs to the Southern Ocean freshwater flux. *JGR Oceans* **111**, C03004 (2006).
34. Sun, S., Eisenman, I. & Stewart, A. L. Does Southern Ocean surface forcing shape the global ocean overturning circulation? *Geophys. Res. Lett*. **45**, 2413–2423 (2018).
35. Gordon, A. L. Interocean exchange of thermocline water. *J. Geophys. Res*. **91**, 5037–5046 (1986).
36. Scussolini, P., Marino, G., Brummer, G. J. A. & Peeters, F. J. Saline Indian Ocean waters invaded the South Atlantic thermocline during glacial termination II. *Geology* **43**, 139–142 (2015).
37. Seidov, D., Stouffer, R. J. & Haupt, B. J. Is there a simple bi-polar ocean seesaw? *Glob. Planet. Change* **49**, 19–27 (2005).
38. Stouffer, R. J., Seidov, D. & Haupt, B. J. Climate response to external sources of freshwater: North Atlantic versus the Southern Ocean. *J. Clim*. **20**, 436–448 (2007).
39. Schmittner, A. Southern Ocean sea ice and radiocarbon ages of glacial bottom waters. *Earth Planet. Sci. Lett*. **213**, 53–62 (2003).
40. Menviel, L. et al. Poorly ventilated deep ocean at the Last Glacial Maximum inferred from carbon isotopes: a data-model comparison study. *Paleoceanography* **32**, 2–17 (2017).
41. Molyneux, E. G., Hall, I. R., Zahn, R. & Diz, P. Deep water variability on the southern Agulhas Plateau: interhemispheric links over the past 170 ka. *Paleoceanography* **22**, PA4209 (2007).
42. Imbrie, J. et al. On the structure and origin of major glaciation cycles 1. Linear responses to Milankovitch forcing. *Paleoceanography* **7**, 701–738 (1992).
43. Brathauer, U. & Abelmann, A. Late quaternary variations in sea surface temperatures and their relationship to orbital forcing recorded in the Southern Ocean (Atlantic sector). *Paleoceanography* **14**, 135–148 (1999).
44. Venz, K. A., Hodell, D. A., Stanton, C. & Warnke, D. A. A 1.0 Myr record of Glacial North Atlantic Intermediate Water variability from ODP site 982 in the northeast Atlantic. *Paleoceanography* **14**, 42–52 (1999).
45. Timmermann, A. et al. Modeling obliquity and CO_2 effects on Southern Hemisphere climate during the past 408 ka. *J. Clim*. **27**, 1863–1875 (2014).
46. Romero, O. E. et al. High-latitude forcing of diatom productivity in the southern Agulhas Plateau during the past 350 kyr. *Paleoceanography* **30**, 118–132 (2015).
47. Willeit, M., Ganopolski, A., Calov, R. & Brovkin, V. Mid-Pleistocene transition in glacial cycles explained by declining CO_2 and regolith removal. *Sci. Adv*. **5**, eaav7337 (2019).
48. Rodríguez-Sanz, L., Graham Mortyn, P., Martínez-Garcia, A., Rosell-Melé, A. & Hall, I. R. Glacial Southern Ocean freshening at the onset of the Middle Pleistocene Climate Transition. *Earth Planet. Sci. Lett*. **345–348**, 194–202 (2012).
49. Raymo, M. E., Lisiecki, L. E. & Nisancioglu, K. H. Plio-pleistocene ice volume, Antarctic climate, and the global $\delta^{18}O$ record. *Science* **313**, 492–495 (2006).
50. Pena, L. D. & Goldstein, S. L. Thermohaline circulation crisis and impacts during the mid-Pleistocene transition. *Science* **345**, 318–322 (2014).
51. Graham, R. M. & De Boer, A. M. The dynamical subtropical front. *JGR Oceans* **118**, 5676–5685 (2013).
52. Laskar, J. et al. A long-term numerical solution for the insolation quantities of the Earth. *Astron. Astrophys*. **428**, 261–285 (2004).

Expedition 361 Science Party

Ian R. Hall[1], Sidney R. Hemming[5], Leah J. LeVay[13], Stephen Barker[1], Melissa A. Berke[7], Luna Brentegani[16], Thibaut Caley[17], Alejandra Cartagena-Sierra[7], Christopher D. Charles[18], Jason J. Coenen[19], Julien G. Crespin[17], Allison M. Franzese[20], Jens Gruetzner[2], Xibin Han[21], Sophia K. V. Hines[5], Francisco J. Jimenez Espejo[9,10], Janna Just[22], Andreas Koutsodendris[23], Kaoru Kubota[24], Nambiyathodi Lathika[12], Richard D. Norris[18], Thiago Pereira dos Santos[25], Rebecca S. Robinson[14], John M. Rolison[26], Margit H. Simon[27], Deborah Tangunan[28], H. J. L. van der Lubbe[1,6], Masako Yamane[10] & Hucai Zhang[29]

[16]Earth and Environmental Sciences, University of Technology Queensland, Brisbane, Queensland, Australia. [17]EPOC, UMR CNRS 5805, University of Bordeaux, Pessac, France. [18]Scripps Institution of Oceanography, University of California, San Diego, La Jolla, CA, USA. [19]Department of Geology, Northern Illinois University, Sycamore, IL, USA. [20]Natural Sciences Department, School of Earth and Environmental Sciences, Hostos Community College (C.U.N.Y.), Bronx, NY, USA. [21]Second Institute of Oceanography (SOA), Key Laboratory of Submarine Science, Hangzhou, People's Republic of China. [22]Geologisches Institut, Universität Köln, Cologne, Germany. [23]Institute of Earth Sciences, University of Heidelberg, Heidelberg, Germany. [24]Atmosphere and Ocean Research Institute, University of Tokyo, Kashiwashi, Japan. [25]Institute for Geosciences, Universidade Federal Fluminense (UFF), Rio de Janeiro, Brazil. [26]Chemistry Department, University of Otago, Dunedin, New Zealand. [27]Bjerknes Centre for Climate Research, Bergen, Norway. [28]Department of Geosciences, University of Bremen, Bremen, Germany. [29]Laboratory of Plateau Lake Ecology and Global Change, Yunnan Normal University, Kunming, People's Republic of China.

Methods

AP_{comp}

The Agulhas Plateau composite (AP_{comp}) is a stratigraphic framework consisting of proximal sediment core sites MD02-2588 (41° 19.90′ S, 25° 49.7′ E, 2,907 m) and IODP site U1475 (41° 25.6′ S, 25° 15.6′ E, 2,669 m). We use existing records from the upper 10.27 m of MD02-2588 ($\delta^{18}O_{benthic}$ and $\delta^{13}C_{benthic}$ from ref. [13], IRD counts from ref. [11]) and correlated the lowest deglaciation in MD02-2588 to the respective deglaciation in site U1475 using $\delta^{18}O_{benthic}$ and $\delta^{13}C_{benthic}$ from both cores. This tie point is at 10.27 m in MD02-2588 and 8.16 m on the U1475 Splice (Extended Data Fig. 2a). The chronology is based on graphically aligning $\delta^{18}O_{benthic}$ to the 'Prob-stack' (a probabilistic stack of $\delta^{18}O_{benthic}$ using a profile-hidden Markov model)[53]. The Prob-stack includes 180 globally distributed $\delta^{18}O_{benthic}$ records and provides an update of the LR04 stack and timescale[54]. The Prob-stack and LR04 are similar over the MPT interval studied here. From selected age-depth markers ($n = 45$; consisting of 12 radiocarbon dates and 33 $\delta^{18}O_{benthic}$ ties points; Extended Data Fig. 2b), the final age-depth model was constructed using the deterministic age modelling routine Undatable[55] with 10^5 bootstrap simulations. The resultant sedimentation rates range from 1.2 cm kyr^{-1} to 7.6 cm kyr^{-1}, averaging 3.1 cm kyr^{-1}. The Brunhes–Matuyama magnetic reversal (0.781 Ma) and the Jaramillo Subchron (1.072–0.988 Ma) are identified in the U1475 down-core magnetic inclination[56], confirming the robustness of the final age–depth model. The records presented have a temporal resolution ranging from approximately 0.3 kyr in the Late Pleistocene to approximately 1.5 kyr in the early-to-mid Pleistocene. Stable isotope measurements were performed on 2–3 well preserved *C. wuellerstorfi* specimens (250–315 µm size fraction) and performed at Cardiff University using a Thermo Finnigan MAT 253 mass spectrometer linked online to a Carbo Kiel carbonate preparation device with long-term precision of ±0.05‰ for $\delta^{18}O$ and ±0.021‰ for $\delta^{13}C$ (±1σ). Results are calibrated to an internal laboratory standard (BCT63) and presented relative to the Vienna Pee Dee belemnite scale.

Ice-rafted debris

IRD_{MAR} was determined by counting detrital mineral grains in the >150 µm sediment fraction (subsampled using a micropalaeontology splitter to yield 500–1,000 entities) before normalization to sample weight (IRD concentration in number of grains per gram of dry sediment) and then multiplication by apparent bulk mass-accumulation rate (MAR; Extended Data Fig. 2c), derived from estimates of dry bulk density from[57] and linear sedimentation rate. The temporal evolution, spectral characteristics and timing of peaks in the IRD record are largely unaffected by conversion from concentration to MAR. This methodology is equivalent to that used for MD02-2588 (the measurements for which were previously published[11,12], $n = 522$); however, as no dry-bulk density (DBD) data are available for MD02-2588, we estimate it using a second-order polynomial fitted to DBD in the overlapping interval of site U1475: $DBD = -0.0003x^2 + 0.0161x + 0.7122$; where x is depth in cm. We chose this method to attempt to account for the downcore trend of increasing DBD in site U1475; however, we emphasize that the result from this approach is similar to the result from simply taking the mean DBD from site U1475—for example, 0.9 g cm^{-3} (polynomial approach) versus 0.86 g cm^{-3} (mean approach) at a depth of 0.5 cm in MD02-2588.

No quantitative distinction is presented between mineralogies of phenocrysts present; however, grains that were clearly of volcanic (for example, tephra) or authigenic (for example, pyrite) were excluded from the IRD counts. Energy dispersive X-ray spectrometry (EDS) point analysis was used to identify the mineralogy of several grains from a selection of samples (total grains = 31). Of the 31 measured, 23 were quartz (mostly 'clean' quartz with some Fe–K and Fe members), seven were orthoclase (K-feldspar), and one was garnet (almandine member) (Extended Data Fig. 3). The origin of ice-rafted minerals in the Atlantic Southern Ocean has been the topic of some discussion, as the presence of sea-ice rafted volcanic and mafic material in sediment cores close to volcanic subantarctic islands can complicate the interpretation of IRD records[58,59]. However, the observed AP_{comp} assemblage of predominantly quartz with some K-feldspar and garnet is distinct from the plagioclase-dominated clear mineral assemblages found close to Bouvet Island[25,59]. This mineralogy implies a continental Antarctic origin[60]: the high quartz proportion may suggest a Ronne Ice Shelf, Filchner Ice Shelf or Antarctic Peninsula origin[60], although the presence of garnet indicates an East Antarctic contribution[25,60]. Micro-textures such as striations and step-like fractures identified on selected quartz grains further support a glacial origin[61].

Climate model experiments

We use a comprehensive fully coupled atmosphere–ocean general circulation model (AOGCM), COSMOS (ECHAM5-JSBACH-MPI-OM) in this study. The atmospheric model ECHAM5[62], complemented by the land surface component JSBACH[63], is used at T31 resolution (3.75°), with 19 vertical layers. The ocean model MPI-OM[64], including sea-ice dynamics that is formulated using viscous-plastic rheology[65], has a resolution of GR30 (3° × 1.8°) in the horizontal, with 40 uneven vertical layers. The climate model has already been used to investigate a range of palaeoclimate phenomena[15,66,67]. This indicates that it can capture key features of warm and cold climate and is thus a very suitable climate model for this study, especially glacial Southern Ocean conditions and AABW formation[15]. In this study, to investigate responses of Antarctic iceberg transport to different climate backgrounds of the Southern Ocean, we used published equilibrium experiments under pre-industrial and LGM boundary conditions[15]. To further assess roles of a lower-than-LGM obliquity (that is, additional cooling on the glacial Southern Ocean), we further conducted one LGM sensitivity experiment with 27-kyr obliquity (22.25°) that is lower than the LGM value (22.949°). The three experiments are integrated to quasi-equilibrium and the average of the last 100 years is calculated to represent the corresponding climatology and used for modelling iceberg trajectory. The simulated climatological Southern Ocean conditions of these runs can be found in Extended Data Fig. 6.

Iceberg trajectory model

We use Pyberg (https://github.com/trackow/pyberg), an offline Python implementation of the FESOM-IB iceberg drift and decay module[14]. The model simulates iceberg trajectories and along-track rates of melting using established iceberg physics[68–70]. Pyberg reads monthly forcing data from different climates as simulated by the COSMOS climate model (10 m winds and ocean currents for atmospheric and oceanic drags, sea surface height for the surface slope term, sea surface temperature for melting parametrizations). Monthly sea-ice fields are also read and allowed to lock icebergs into the sea ice when ice concentrations exceed 86%[29,70]. In that case, icebergs are advected along with the sea-ice velocity field. Erosion of icebergs by surface waves is damped at high ice concentrations[69]. Pyberg uses the constant density roll-over criterion (equation 3 in ref. [71]), which can be viewed as a more physical version of the widely adopted original formulation[72]. Iceberg fracture is not included, because parametrization of this process for climate models is still an active area of research[73,74].

Icebergs are initialized between 63 °W–50 °W in the iceberg alley of the Weddell Sea from an observationally derived modern distribution of near-coastal iceberg positions and horizontal sizes (ref. [75]; https://doi.org/10.1594/PANGAEA.843280). The initial iceberg height is set to 250 m and the density to 850 kg m^3 (refs. [33,75,76]). The total initial iceberg mass in the iceberg alley is thus 49.59 Gt. For consistency, and to start the icebergs within the ocean model domain, the initial positions are shifted 10° to the East for all experiments to account for the larger spatial extent of the Antarctic Ice Sheet during the LGM. Along-track melt-rates are gridded and summed on a 1°× 1° regular grid to produce the meltwater distribution. The modelled pre-industrial trajectories

are consistent with modern observational datasets[29,30] (Extended Data Fig. 7). The LGM results are broadly consistent with the previously published results from the Fine Resolution Greenland and Labrador (FRUGAL) intermediate complexity climate model iceberg module[16], with an equatorward shift and lengthening of trajectories in the Atlantic–Indian Southern Ocean sector, however discrepancies are apparent such as the more extreme equatorward spread of LGM trajectories in the FRUGAL model compared to Pyberg. This is the result of different iceberg seeding configurations (that is, we introduce icebergs only in the 'iceberg alley' region and neglect possible subantarctic sources) and variations in the forcing provided by the underlying climate models. We note that our interpretations based on the Pyberg results are entirely compatible with the results from FRUGAL, and the results of the latter suggest that our estimated meltwater redistribution is probably conservative. Furthermore, the Pyberg LGM results are supported by available IRD records from the Southern Ocean[22–25,77,78], which typically show a latitudinal divide between higher (lower) IRD accumulation close to (away from) Antarctica during glacial compared to interglacial intervals.

Water-mass mixing model

To identify the water mass signal on the AP_{comp} $\delta^{13}C_{benthic}$, we apply a simple binary mixing model[79] to estimate the percentage of NSW from stacked $\delta^{13}C_{benthic}$ records representing NSW and SSW over the past 1.5 Myr:

$$\%\mathrm{NSW} = 100 \times \frac{\delta^{13}C_{\mathrm{APcomp}} - \delta^{13}C_{\mathrm{SSW}}}{\delta^{13}C_{\mathrm{NSW}} - \delta^{13}C_{\mathrm{SSW}}}.$$

Here $\delta^{13}C_{NSW}$ is a shallow North Atlantic stack (consisting of ODP sites 980, 982, 983)[80], and $\delta^{13}C_{SSW}$ is a deep South Atlantic stack (consisting of ODP sites 1089 and 1090)[81]. Stacks were created by converting all data onto the LR04[54] timescale, smoothing with a 5-kyr Gaussian filter, and averaging. We apply this technique using both an SSW stack and a PDW stack as the second end-member, as in reality the 'southern' deep-water mass present in the glacial Atlantic is probably some combination of the two. For example, although several studies employ a PDW end-member[79,82,83], another work[82] notes that this is due to the absence of suitable Southern Ocean end-member records. A later study[84] applies the same approach with newly available deep Southern Ocean $\delta^{13}C_{benthic}$ records. However, recent evidence indicates that PDW was present in the glacial Atlantic Ocean in larger proportions than previously thought[85] and so a PDW end-member may be preferable after all.

Time-series analysis

The lagged cross-correlation between IRD_{MAR} against $\delta^{18}O_{benthic}$ and $\delta^{13}C_{benthic}$ is determined using the Gaussian-kernel-based cross-correlation algorithm[86] (Extended Data Fig. 5b). This enables cross-correlation analysis to be performed on the original irregularly spaced data, to avoid the possibility of spurious phasing introduced by linear interpolation.

The 'peak-lag' algorithm we design to iteratively measure the offset between peaks in the rate of change of IRD_{MAR} and $\delta^{13}C_{benthic}$ is modified from a previous approach[87] and analogous to 'event synchronization' techniques. The peak-lag algorithm smooths the time series, finds the first difference, and then measures the offset in local maxima of both signals. We tested the sensitivity of the algorithm to the smoothing filter selection, finding that the average lag computed for a range of filter designs (moving-average and Savitsky–Golay filters; orders between 1 and 21) give similar results within 1σ of each other. We additionally test the confidence that the result from our final chosen parameters (seven-point moving-average) is significantly non-zero by performing 1,000 Monte Carlo simulations with zero-lag red noise surrogates (generated from an autoregressive model of the real data), finding that the lag identified in our data (IRD_{MAR} versus $\delta^{13}C_{benthic}$) is significantly different from the surrogate series ($n = 1{,}000$, $P < 10^{-10}$); this additionally yields a 99% red-noise confidence level of ±0.4 kyr for the lag calculated for our data. We test the utility of the algorithm to detect lead–lag relationships in a series of surrogate time series with known lags applied by constructing synthetic time series from three sine waves (100, 41, 23-kyr periods), with higher-frequency oscillation (7-kyr period) and white-noise components added to emulate suborbital features. Known lags are imposed between pairs of the surrogate series. The results show that the algorithm performs well and is capable of detecting a lag of down to 0.4 kyr to a confidence of $P < 10^{-10}$. The algorithm shows an inherent drift at higher lags (Extended Data Fig. 5a and b), meaning it underestimates lag times greater than 4 kyr, however the 1.5-kyr lag observed in our data should be short enough to be unaffected by this drift.

To divide the time series into glacial cycles (as in Fig. 4) we define intervals between peak interglacial conditions (identified as local minima in $\delta^{18}O_{benthic}$ separated by a minimum distance of 25 kyr) and the next time $\delta^{18}O_{benthic}$ crosses an 'interglacial threshold' of 3.32‰ (*C. wuellerstorfi* scale, equivalent to 3.75‰ on the LR04-scale). This is lower than previously adopted[88], but ensures that we do not define the interstadial MIS 5c as an interglacial. We manually add a peak interglacial marker at 506 ka (based on Northern Hemisphere perihelion) to include the 'cool' interglacial MIS 13a. Within each interval we calculate the cumulative integral of IRD_{MAR} and $\delta^{18}O_{benthic}$, before normalizing the values to percentages of total 'accumulation' for that interval (Extended Data Fig. 5d).

Finally, for the phase wheels in Fig. 3, we use the Blackman–Tukey method with a Bartlett window (using the Analyseries software[89]) after linearly interpolating (time step of 1.5 kyr) and standardizing (mean = 0, standard deviation = 1) the data.

Orbital forcing and the MPT

We estimate the time-frequency spectral power in the AP_{comp} IRD_{MAR} time series by applying a continuous wavelet transform[90] (using zero-padding and a Mortlet mother wave). To visualize the results, we extract the power (in units of normalized variance) at the 'Fourier periods' between 39 and 43 kyr^{-1} to represent frequencies associated with obliquity, and 92 to 108 kyr^{-1} to represent frequencies associated with eccentricity (Fig. 4c). We emphasize that this gives an estimate of relative, not absolute, spectral power in these bands. Between 1,600 and approximately 900 ka, the spectral power in the obliquity band is dominant, decreasing after 900 ka in favour of the approximately 100 kyr^{-1} power. This transition then reverses after about 400 ka, when obliquity-band power again dominates. It is important to note that spectral power at frequencies of around 40 kyr^{-1} and 100 kyr^{-1} is not evidence for a direct forcing by the obliquity and eccentricity of Earth's orbit (with dominant periodicities at these values, respectively). Furthermore, it is instructive to also evaluate the timing of cycles in the IRD_{MAR} data relative to cycles in orbital parameters. In Fig. 4b, c, we show that although the spectral power is dominated by approximately 40 kyr^{-1} frequencies (pre- and post-MPT) there is a close coupling between high IRD_{MAR} and low obliquity. A mechanistic relationship here is supported by our climate model results (Extended Data Fig. 6) which indicate that the low obliquity 27-kyr experiment yields cooler Southern Ocean SST and increased sea-ice extent relative to LGM. Indeed, a relationship between obliquity and Southern Ocean sea ice[15,91], as well as stronger westerlies (related to the increased latitudinal insolation gradient[45,92]) has been previously demonstrated; both would act to increase iceberg survivability and transport into and across the SAZ (Extended Data Fig. 7). However, the transient emergence of approximately 100-kyr^{-1} power between around 1.2 Ma and 0.4 Ma coincides with the concealment of this apparent obliquity pacing. Recent modelling results have shown that Southern Ocean sea ice is more sensitive to obliquity than its Northern Hemisphere counterpart[92], and one explanation for the obscuration could be a shift to more complex, nonlinear pacing of

Southern Ocean climate as Northern Hemisphere ice sheets expand and glacial–interglacial variations in atmospheric CO_2 increase[47]. The post-MBE return to obliquity pacing might then indicate a shift in the nature of Northern Hemisphere ice-sheet growth.

Data availability

All newly presented data are available at https://doi.org/10.1594/PANGAEA.921315.

Code availability

Code for all data analysis presented is available at https://github.com/AidanStarr/Starr_et_al_2020 and code for the Pyberg model is available at https://github.com/trackow/pyberg.

53. Ahn, S., Khider, D., Lisiecki, L. E. & Lawrence, C. E. A probabilistic Pliocene–Pleistocene stack of benthic $\delta^{18}O$ using a profile hidden Markov model. *Dyn. Stat. Clim. Syst.* **2**, dzx002 (2017).
54. Lisiecki, L. E. & Raymo, M. E. A Pliocene–Pleistocene stack of 57 globally distributed benthic $\delta^{18}O$ records. *Paleoceanography* **20**, PA1003 (2005); correction **20**, PA2007 (2005).
55. Lougheed, B. C. & Obrochta, S. P. A. Rapid, deterministic age-depth modeling routine for geological sequences with inherent depth uncertainty. *Paleoceanogr. Paleoclimatol.* **34**, 122–133 (2019).
56. Hall, I. R. et al. Site U1475. In *Proc. Int. Ocean Discovery Program* Vol. 361 (eds Hall, I. R. et al.) https://doi.org/10.14379/iodp.proc.361.104.2017 (International Ocean Discovery Program, 2017).
57. Gruetzner, J. et al. A new seismic stratigraphy in the Indian–Atlantic Ocean Gateway resembles major paleo-oceanographic changes of the last 7 Ma. *Geochem. Geophys. Geosyst.* **20**, 339–358 (2019).
58. Kanfoush, S. L. et al. Millennial-scale instability of the Antarctic Ice Sheet during the last glaciation. *Science* **288**, 1815–1819 (2000).
59. Nielsen, S. H., Hodell, D. A., Kamenov, G., Guilderson, T. & Perfit, M. R. Origin and significance of ice-rafted detritus in the Atlantic sector of the Southern Ocean. *Geochem. Geophys. Geosyst.* **8**, Q12005 (2007).
60. Diekmann, B. & Kuhn, G. Provenance and dispersal of glacial–marine surface sediments in the Weddell Sea and adjoining areas, Antarctica: ice-rafting versus current transport. *Mar. Geol.* **158**, 209–231 (1999).
61. St John, K., Passchier, S., Tantillo, B., Darby, D. & Kearns, L. Microfeatures of modern sea-ice-rafted sediment and implications for paleo-sea-ice reconstructions. *Ann. Glaciol.* **56**, 83–93 (2015).
62. Roeckner, E. et al. *The Atmospheric General Circulation Model ECHAM 5. Part I: Model Description*. Report no. 439 (Max-Planck-Institut für Meteorologie, 2003).
63. Brovkin, V., Raddatz, T., Reick, C. H., Claussen, M. & Gayler, V. Global biogeophysical interactions between forest and climate. *Geophys. Res. Lett.* **36**, L07405 (2009).
64. Marsland, S. J., Haak, H., Jungclaus, J. H., Latif, M. & Röske, F. The Max-Planck-Institute global ocean/sea ice model with orthogonal curvilinear coordinates. *Ocean Model.* **5**, 91–127 (2003).
65. Hibler, W. D. A dynamic thermodynamic sea ice model. *J. Phys. Oceanogr.* **9**, 815–846 (1979).
66. Wei, W. & Lohmann, G. Simulated Atlantic multidecadal oscillation during the Holocene. *J. Clim.* **25**, 6989–7002 (2012).
67. Stärz, M., Jokat, W., Knorr, G. & Lohmann, G. Threshold in North Atlantic–Arctic Ocean circulation controlled by the subsidence of the Greenland–Scotland Ridge. *Nat. Commun.* **8**, 15681 (2017).
68. Bigg, G. R., Wadley, M. R., Stevens, D. P. & Johnson, J. A. Modelling the dynamics and thermodynamics of icebergs. *Cold Reg. Sci. Technol.* **26**, 113–135 (1997).
69. Gladstone, R. M., Bigg, G. R. & Nicholls, K. W. Iceberg trajectory modeling and meltwater injection in the Southern Ocean. *JGR Oceans* **106**, 19903–19915 (2001).
70. Lichey, C. & Hellmer, H. H. H. Modeling giant-iceberg drift under the influence of sea ice in the Weddell Sea, Antarctica. *J. Glaciol.* **47**, 452–460 (2001).
71. Wagner, T. J., Stern, A. A., Dell, R. W. & Eisenman, I. On the representation of capsizing in iceberg models. *Ocean Model.* **117**, 88–96 (2017).
72. Weeks, W. F. & Mellor, M. Some elements of iceberg technology. In *Iceberg Utilization*: *Proc. First Int. Conf. Worksh. on Iceberg Utilization for Fresh Water Production, Weather Modification and Other Applications* (ed. Husseiny, A. A.) 45–98 (Pergamon, 1977).
73. Bouhier, N., Tournadre, J., Rémy, F. & Gourves-Cousin, R. Melting and fragmentation laws from the evolution of two large Southern Ocean icebergs estimated from satellite data. *Cryosphere* **12**, 2267–2285 (2018).
74. Wagner, T. J. et al. The "footloose" mechanism: iceberg decay from hydrostatic stresses. *Geophys. Res. Lett.* **41**, 5522–5529 (2014).
75. Wesche, C. & Dierking, W. Near-coastal circum-Antarctic iceberg size distributions determined from synthetic aperture radar images. *Remote Sens. Environ.* **156**, 561–569 (2015).
76. Barbat, M. M., Rackow, T., Hellmer, H. H., Wesche, C. & Mata, M. M. Three years of near-coastal Antarctic iceberg distribution from a machine learning approach applied to SAR imagery. *JGR Oceans* **124**, 6658–6672 (2019).
77. Cooke, D. W. & Hays, J. D. Estimates of Antarctic Ocean seasonal sea-ice cover during glacial intervals. In *Antarctic Geoscience: Symposium on Antarctic Geology and Geophysics* (ed. Craddock, C.) 1017–1025 (1982).
78. Grobe, H. & Mackensen, A. Late Quaternary climatic cycles as recorded in sediments from the Antarctic continental margin. In *The Antarctic Paleoenvironment: A Perspective on Global Change* (eds Kennett, J. P. & Warkne, D. A.) 349–376 (1992).
79. Oppo, D. W. & Fairbanks, R. G. Variability in the deep and intermediate water circulation of the Atlantic Ocean during the past 25,000 years: Northern Hemisphere modulation of the Southern Ocean. *Earth Planet. Sci. Lett.* **86**, 1–15 (1987).
80. Raymo, M. E. et al. Stability of North Atlantic water masses in face of pronounced climate variability during the Pleistocene. *Paleoceanography* **19**, PA2008 (2004).
81. Hodell, D. et al. Data report: oxygen isotope stratigraphy of ODP leg 177 sites 1088, 1089, 1090, 1093, and 1094. In *Proc. ODP Sci. Res.* Vol. 177 (eds Gersonde, R. et al.) Ch. 9 (2003).
82. Raymo, M. E., Oppo, D. W. & Curry, W. The mid-Pleistocene climate transition: a deep sea carbon isotopic perspective records from the deep ocean, extending back examined in order to constrain decrease in mean. *Paleoceanography* **12**, 546–559 (1997).
83. Lang, D. C. et al. Incursions of southern-sourced water into the deep North Atlantic during late Pliocene glacial intensification. *Nat. Geosci.* **9**, 375–379 (2016).
84. Venz, K. A. & Hodell, D. A. New evidence for changes in Plio–Pleistocene deep water circulation from Southern Ocean ODP leg 177 site 1090. *Palaeogeogr. Palaeoclimatol. Palaeoecol.* **182**, 197–220 (2002).
85. Yu, J. et al. Last glacial atmospheric CO_2 decline due to widespread Pacific deep-water expansion. *Nat. Geosci.* **13**, 628–633 (2020).
86. Rehfeld, K., Marwan, N., Heitzig, J. & Kurths, J. Comparison of correlation analysis techniques for irregularly sampled time series. *Nonlinear Process. Geophys.* **18**, 389–404 (2011).
87. Barker, S. et al. Icebergs not the trigger for North Atlantic cold events. *Nature* **520**, 333–336 (2015).
88. Past Interglacials Working Group of PAGES. Interglacials of the last 800,000 years. *Rev. Geophys.* **54**, 162–219 (2016).
89. Paillard, D., Labeyrie, L. & Yiou, P. Macintosh program performs time-series analysis. *Eos* **77**, 379 (1996).
90. Grinsted, A., Moore, J. C. & Jevrejeva, S. Application of the cross wavelet transform and wavelet coherence to geophysical time series. *Nonlinear Process. Geophys.* **11**, 561–566 (2004).
91. Fogwill, C. J., Turney, C. S., Hutchinson, D. K., Taschetto, A. S. & England, M. H. Obliquity control on Southern Hemisphere climate during the last glacial. *Sci. Rep.* **5**, 11673 (2015).
92. Wu, Z., Yin, Q., Guo, Z. & Berger, A. Hemisphere differences in response of sea surface temperature and sea ice to precession and obliquity. *Glob. Planet. Change* **192**, 103223 (2020).
93. Marshall, J. & Speer, K. Closure of the meridional overturning circulation through Southern Ocean upwelling. *Nat. Geosci.* **5**, 171–180 (2012).
94. Eide, M., Olsen, A., Ninnemann, U. S. & Johannessen, T. A global ocean climatology of preindustrial and modern ocean $\delta^{13}C$. *Glob. Biogeochem. Cycles* **31**, 515–534 (2017).
95. Budge, J. S. & Long, D. G. A comprehensive database for Antarctic iceberg tracking using scatterometer data. *IEEE J. Sel. Top. Appl. Earth Obs. Remote Sens.* **11**, 434–442 (2018).

Acknowledgements This research used samples and/or data provided by the International Ocean Discovery Program (IODP). Funding for this research was provided by The Natural Environmental Research Council GW4+ Doctoral Training Partnership (A.S.) and NERC grant NE/P000037/1 (I.R.H.). A.S. acknowledges further funding through the Antarctic Science International Bursary. X.Z. acknowledges funding from Lanzhou University (number 225000-830006) and National Key R&D programme of China (number 2018YFA0606403). F.J.J.-E. acknowledges funding through Spanish Ministry of Science and Innovation (grant CTM2017-89711-C2-1-P), co-funded by the European Union through FEDER funds. G.K. acknowledges funding by the German Helmholtz national REKLIM initiative and the BMBF project PalMod. L. Owen, S. Slater, A. Nedebragt and D. Muir are thanked for laboratory assistance.

Author contributions IODP Expedition 361 was led by I.R.H. and S.R.H. All Expedition 361 Science Party members contributed to sample collection. I.R.H. formulated the research. A.S. performed laboratory analysis. A.S. performed data analysis with input from S.B., I.R.H., G.K., and H.J.L.v.d.L. T.R. performed Pyberg experiments and X.Z. performed COSMOS experiments. A.S. wrote the manuscript with input from I.R.H., S.B., G.K., T.R. and X.Z. All authors contributed to the interpretation of results and commented on the final manuscript.

Competing interests The authors declare no competing interests.

Additional information

Correspondence and requests for materials should be addressed to A.S. or I.R.H.

Peer review information *Nature* thanks Helen Bostock, Till Wagner and the other, anonymous, reviewer(s) for their contribution to the peer review of this work.

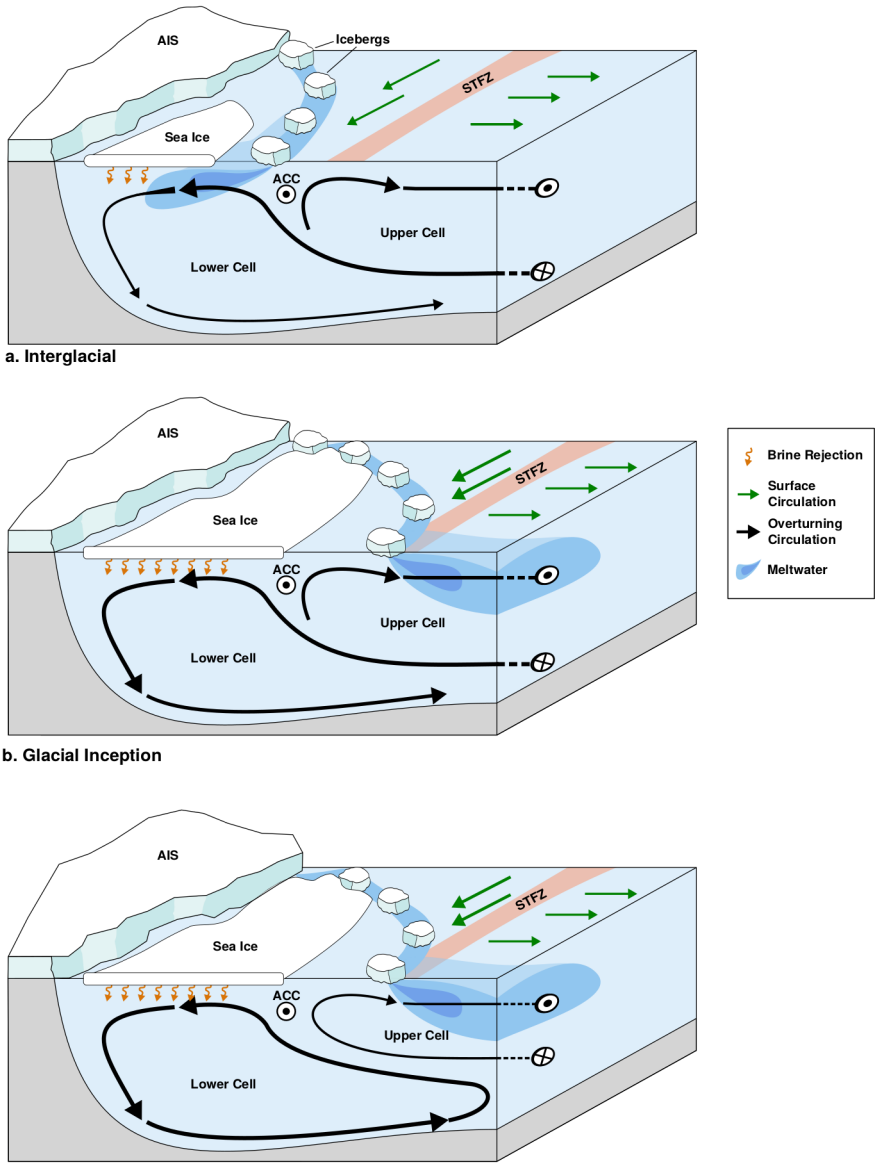

Extended Data Fig. 1 | Schematic representation of the 'southern escape' mechanism described in this study. a, An idealized representation of the Southern Ocean during interglacial conditions. The front-facing panel gives meridional-averaged overturning circulation[93], with circulation divided into an upper cell and lower cell. Arrow width represents the relative strength of each circulation cell (wider being stronger). The top panel represents the ocean surface, with icebergs calving from the Antarctic Ice Sheet (AIS) and following a northward then eastward trajectory. The blue shading represents iceberg meltwater being entrained into the lower cell as icebergs melt south of the main Antarctic Circumpolar Current (ACC) belt. Orange wavy arrows represent brine rejection from sea-ice formation. The peach-coloured band represents the subtropical frontal zone (STFZ) delineating the subtropical regime to the north and the (sub)Antarctic regime to the south. **b**, As in **a**, for conditions during glacial inception; that is, the transition from interglacial to glacial conditions. The major change from **a** is the northward displacement of iceberg trajectories, resulting in much of the meltwater spreading northwards and being entrained in the upper cell, instead of the lower cell. Second, colder surface conditions facilitate extended sea-ice cover, and subsequent increase in brine rejection. The lower cell experiences less-positive buoyancy forcing from the combination of less iceberg meltwater and more brine rejection, and thus becomes stronger. The southern escape of meltwater into the upper cell has not yet occurred in high enough amounts to perturb the upper cell and hence the geometries of the overturning cells are unchanged from **a**. **c**, As in **a** and **b**, for full glacial conditions (occurring after **b**.). Here the southern escape of meltwater has successfully perturbed the upper cell, which is now weaker and has contracted upwards. The now-dominant lower cell has thus increased in volume.

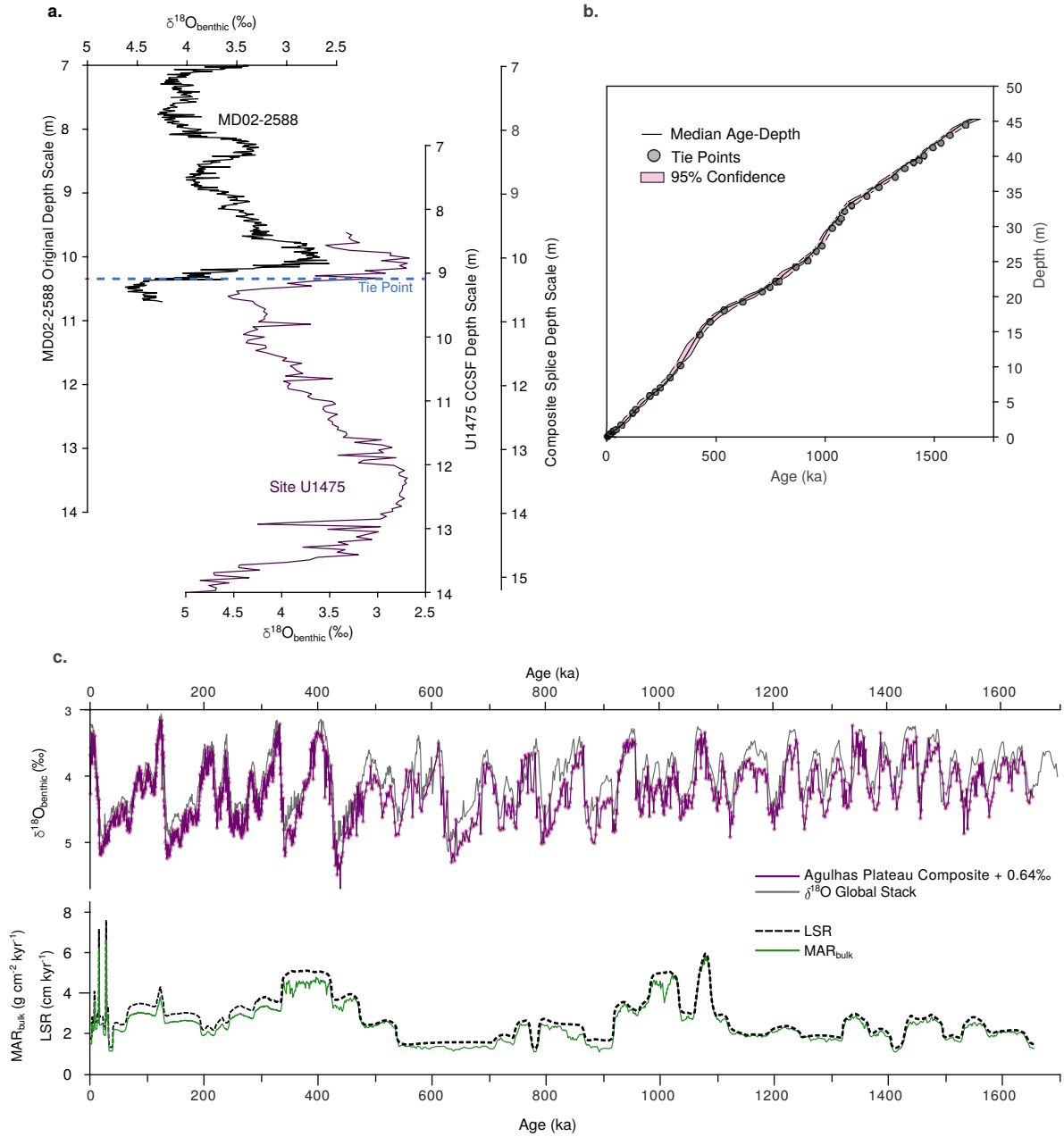

Extended Data Fig. 2 | AP_{comp} age model and composite record construction. a, The appending of U1475 to the bottom of MD02-2588 using $\delta^{18}O_{benthic}$ with the new AP_{comp} composite depth scale on the right-hand axis. **b**, Age-depth tie points (circles) with the median and 95% confidence bounds for the deterministic age model. Depth is given on the AP_{comp} scale. **c**, The $\delta^{18}O_{benthic}$ from this study (purple) and the tuning target, the global $\delta^{18}O_{benthic}$ stack[53] (light grey), and the implied linear sedimentation rates (black dashed line) and calculated MAR (green solid line) from the final age model in the lower subplot.

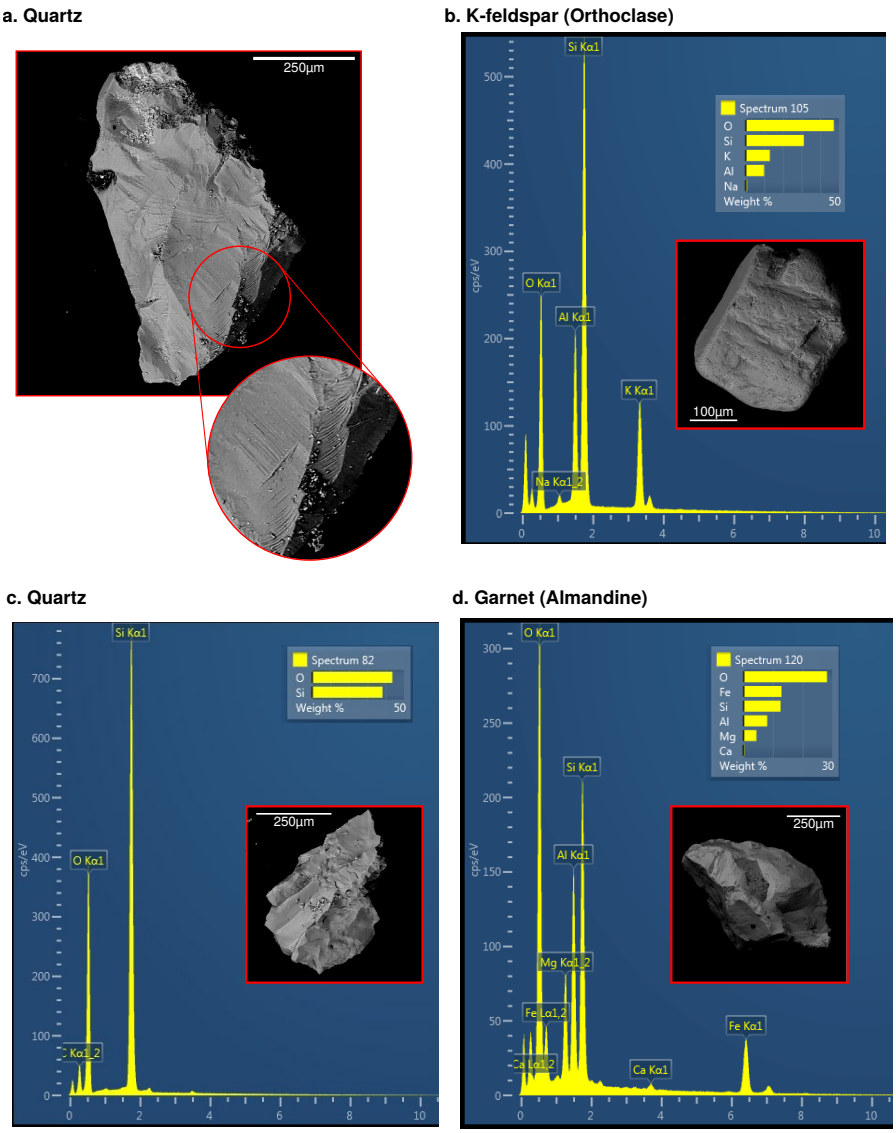

Extended Data Fig. 3 | SEM imaging and mineralogy of IRD grains from the AP_{comp}. **a**, An SEM image of a quartz grain from site U1475 with an enlarged view of surface microtextures in the inset panel. **b**–**d**, SEM images of IRD grains with examples of relative peak intensities for elements derived from EDS point analyses. The images show spectra typical of quartz (**b**), of garnet (almandine member; **c**) and of K-feldspar (orthoclase; **d**). Scale bars are given in white on all SEM images.

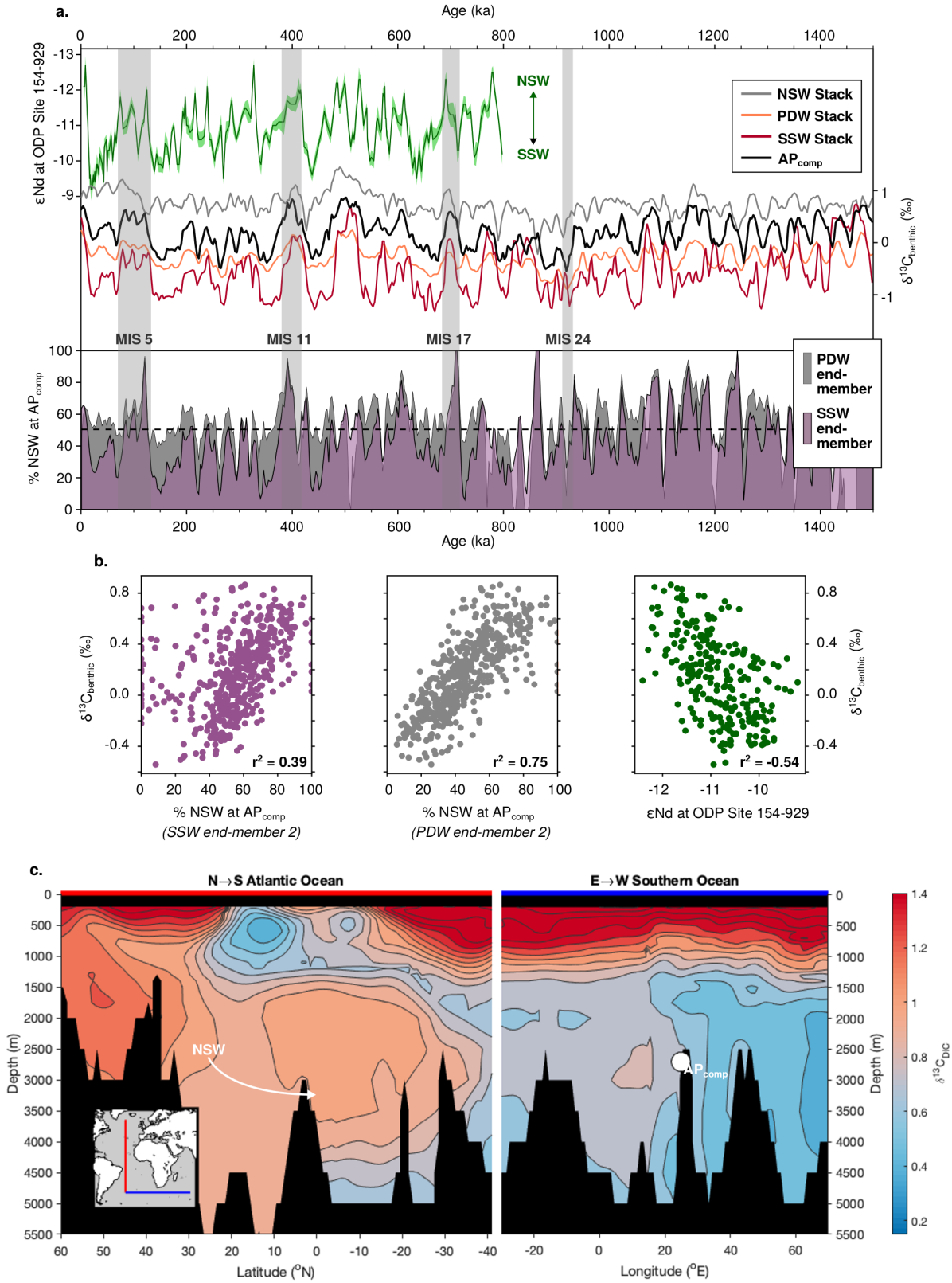

Extended Data Fig. 4 | Comparison of $\delta^{13}C_{benthic}$ and water mass 'end-members'. **a**, Authigenic εNd ($^{143}Nd/^{144}Nd$) isotope record from the deep equatorial Atlantic (ODP site 154-929 from ref. [20]; top, green), Smoothed $\delta^{13}C_{benthic}$ stacks for northern-sourced water (NSW), Pacific deep water (PDW) and southern-sourced water (SSW) end-members (see Methods for stack construction and constituent core sites) and the AP$_{comp}$ $\delta^{13}C_{benthic}$ record. Selected MISs are shown as grey vertical shading. The bottom time series in **a** shows %NSW at the AP$_{comp}$ calculated using a binary mixing model with NSW and a PDW (grey) or SSW (purple) end-members. **b**, Scatter plots of AP$_{comp}$ $\delta^{13}C_{benthic}$ versus %NSW calculated with an SSW (left) and PDW (middle) end-member, and versus the εNd isotope record of ref. [20] (right). Pearson's correlation coefficient, r^2, is given. **c**, Pre-industrial $\delta^{13}C$ of dissolved organic carbon (from ref. [94]) along a north–south (blue) and then east–west (red) transect, with the AP$_{comp}$ position shown as a white circle.

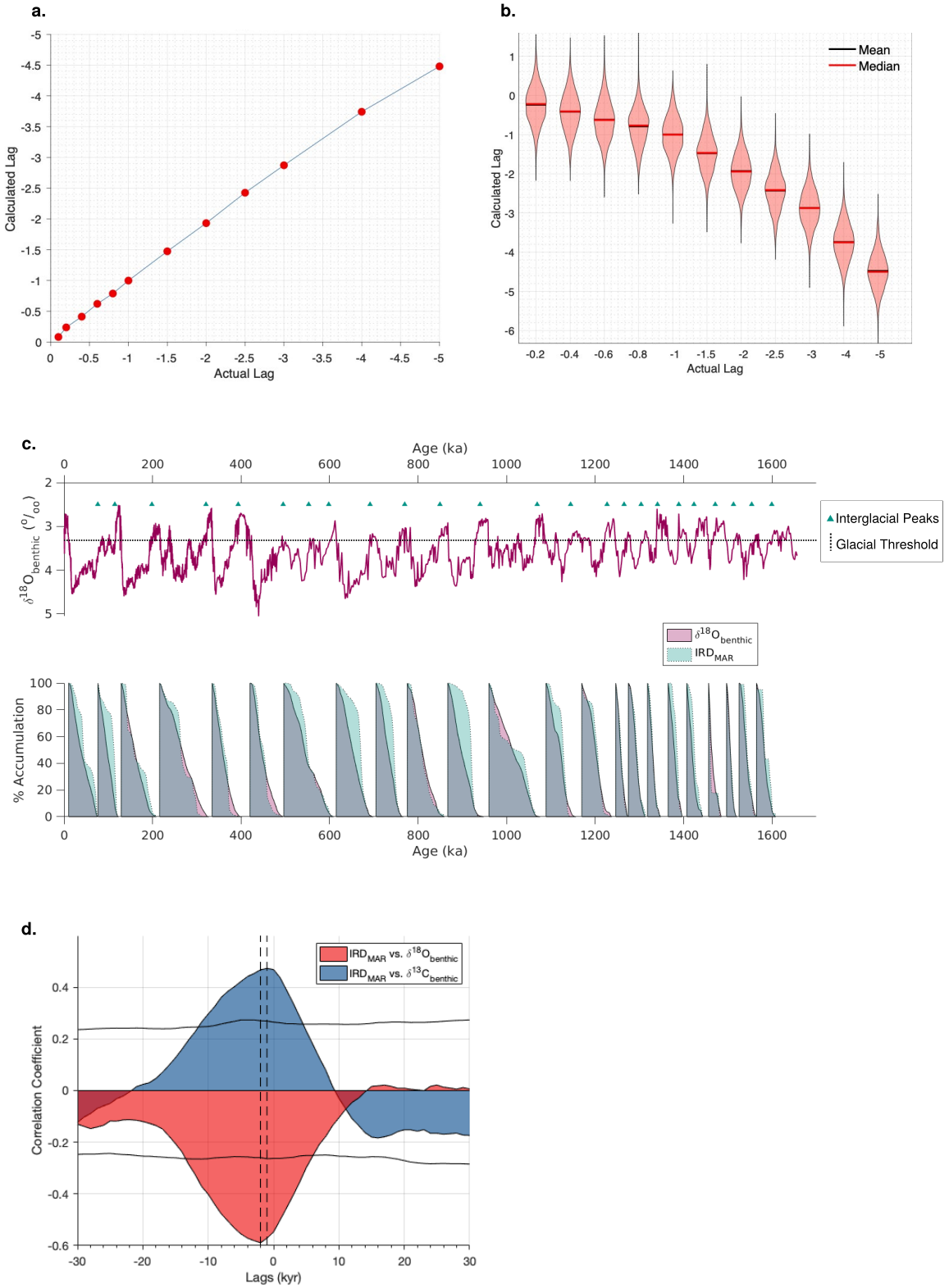

Extended Data Fig. 5 | Time-series analysis algorithm tests. a, **b**, Testing the peak-lag algorithm to detect relationships in a series of surrogate time series with known lags applied. The 'actual lag' axes represent the known lag time imposed between pairs of the surrogate series and the 'calculated lag' axes show the lag estimated by the algorithm. A perfect performance would manifest as a 1:1 straight line through the scatter points. In **b**, the violin plots show the mean, median and kernel probability-density estimates of calculated lags from 10^4 iterations of the test. **c**, Results of the 'glacial accumulation' algorithm with each shaded curve representing IRD_{MAR} (green) and $\delta^{18}O_{benthic}$ (purple) integrated and normalized to 100% within each glacial cycle. Above, the $\delta^{18}O_{benthic}$ record is shown (purple solid line) with green triangles denoting the peak interglacials identified and the dashed black line showing the $\delta^{18}O_{benthic}$ threshold above which the transitions from glacial to interglacial conditions are defined. **d**, Gaussian kernel-based cross-correlation (gXCF)[86] function for AP_{comp} IRD_{MAR} versus $\delta^{13}O_{benthic}$ and $\delta^{13}C_{benthic}$. The horizontal lines show the 95% Monte Carlo confidence levels for significant cross-correlation.

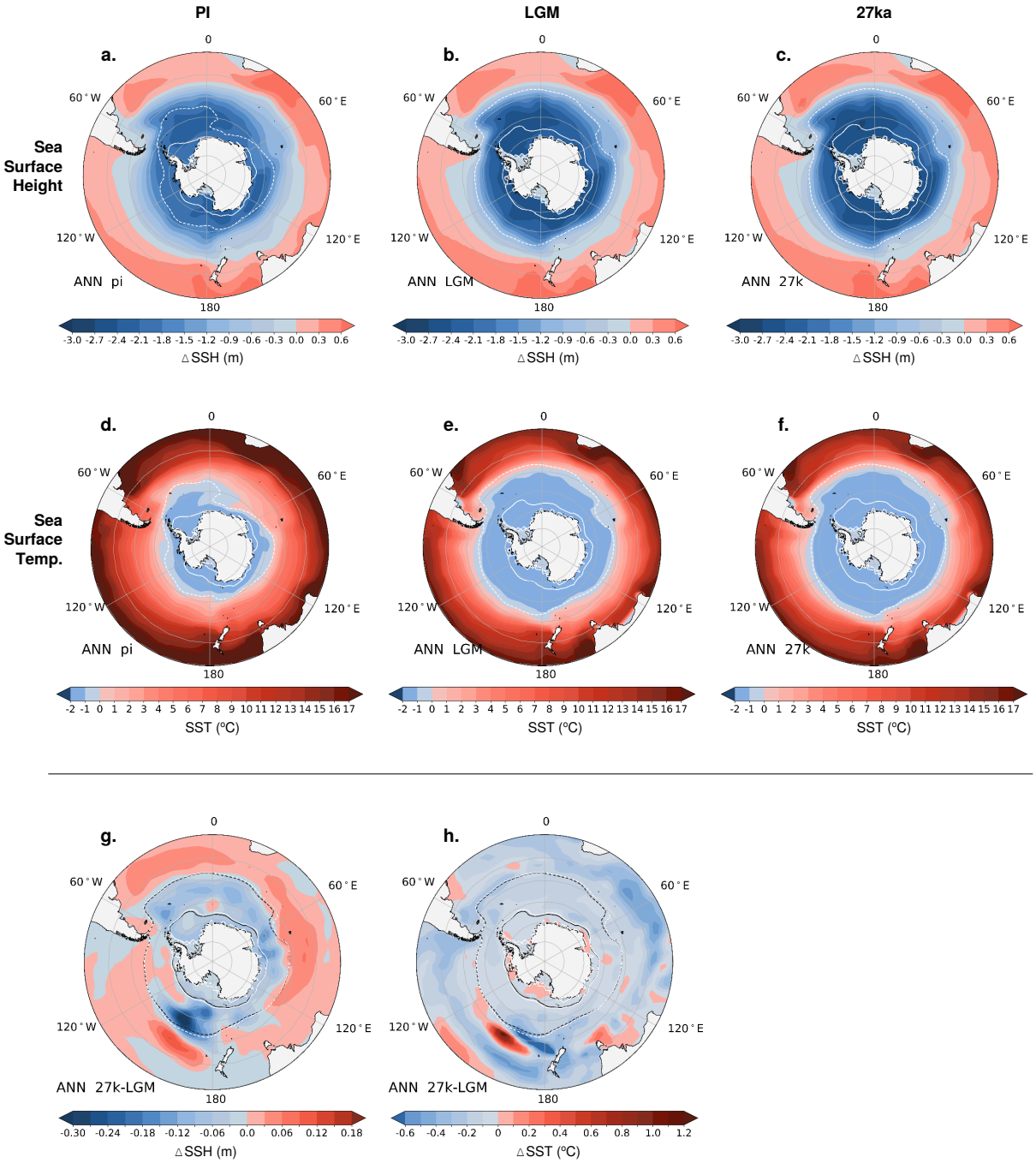

Extended Data Fig. 6 | COSMOS model experiment results. a–**c**, Annual mean sea surface height (SSH; shaded) in experiments for pre-industrial (**a**) LGM (**b**) and 27 ka (**c**). Solid (dashed) contours represent 90% (15%) sea-ice concentration. **d**–**f**, As in **a**–**c**, for climatological annual mean sea surface temperature (SST). **g**, Anomaly of mean annual SSH between 27 ka and LGM experiments. Solid (dashed) contours give 90% (15%) sea-ice concentration (black and white lines represent LGM and 27 ka, respectively). **h**, As in **g**, for SST.

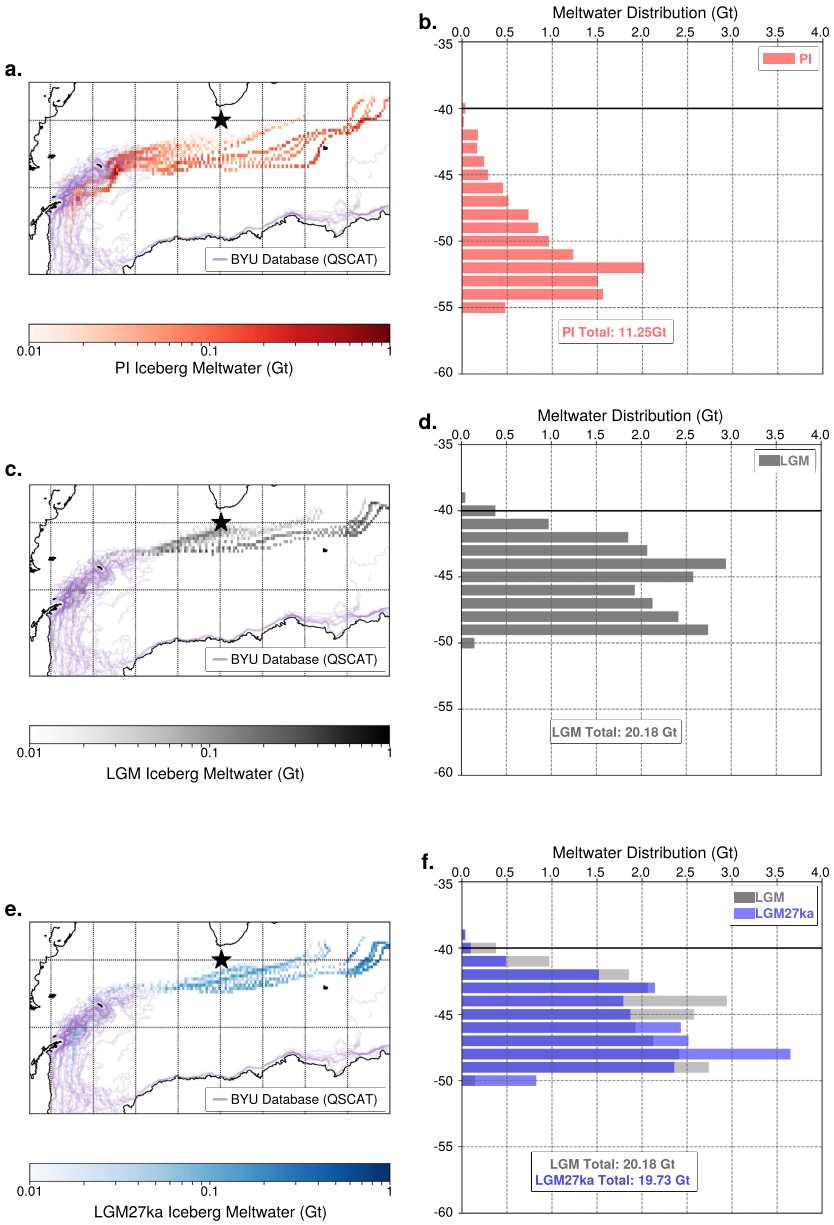

Extended Data Fig. 7 | Pyberg model experiment results. a, **c**, **e**, Spatial distribution of meltwater input estimated for 1° × 1° cells by Pyberg when forced by COSMOS outputs for pre-industrial (PI; **a**), LGM (**c**), and LGM 27 ka (LGM27ka; **e**) conditions. In purple are observed modern iceberg trajectories from the BYU Giant Iceberg database[95] (QSCAT); the modelled pre-industrial trajectories appear substantially longer than the observed, probably because icebergs are tracked in Pyberg even after they become too small to be identified and hence tracked by modern observational techniques. **b**, **d**, **f**, Zonally averaged meltwater estimates for pre-industrial (**b**), LGM (**d**) and LGM27ka (**f**) experiments. The average is taken for each latitude between 0 and 50° E; in other words, this shows the latitudinal distribution of meltwater across the Indian–Atlantic Ocean Gateway.